In the format provided by the authors and unedited.

Fast, in vivo voltage imaging using a red fluorescent indicator

Madhuvanthi Kannan [1,2,3,7], **Ganesh Vasan** [1,2,3,7], **Cheng Huang** [4], **Simon Haziza** [4], **Jin Zhong Li**[4,5], **Hakan Inan** [4], **Mark J. Schnitzer**[4,5,6] **and Vincent A. Pieribone** [1,2,3]★

---

[1]The John B. Pierce Laboratory, New Haven, CT, USA. [2]Department of Cellular and Molecular Physiology, Yale University, New Haven, CT, USA. [3]Department of Neuroscience, Yale University, New Haven, CT, USA. [4]James H. Clark Center, Stanford University, Stanford, CA, USA. [5]CNC Program, Stanford University, Stanford, CA, USA. [6]Howard Hughes Medical Institute, Stanford University, Stanford, CA, USA. [7]These authors contributed equally: Madhuvanthi Kannan and Ganesh Vasan. *e-mail: vincent.pieribone@yale.edu
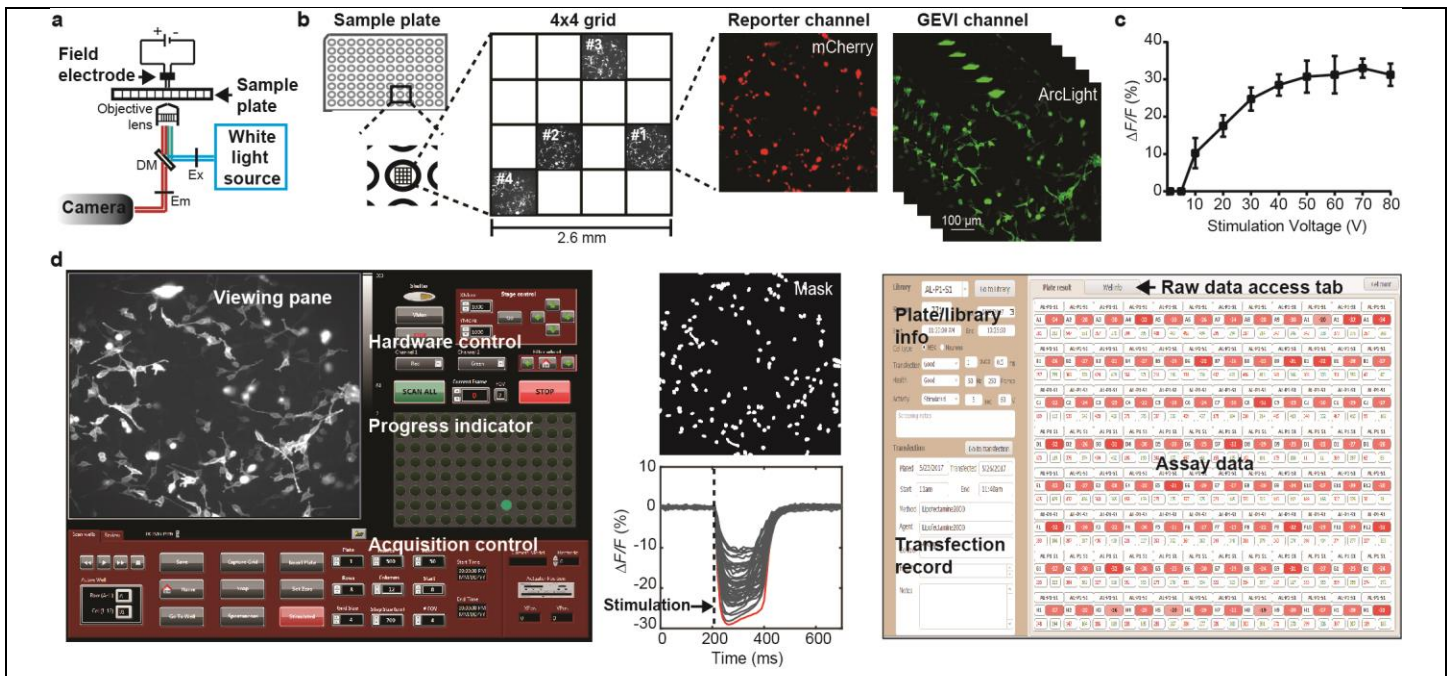
Supplementary Figure 1

Voltage screening, data analysis and management on the high-throughput platform.

(**a**) Schematic of optical and electrical setup. Each well of the sample plate is sequentially aligned along the light path and cells are stimulated by a single field electrode. A white light source is used for sample illumination and fluorescence emission is collected by a high-resolution camera. Ex and Em denote excitation and emission filters; DM, dichroic mirror. (**b**) Schematic of image acquisition. In each well, images (reporter channel) are captured in 16 fields of view (FOVs) in a 4 × 4 grid, and ranked by transfection density. Time-series images in the GEVI channel are acquired in the top four FOVs following field stimulation. (**c**) Fluorescence responses of ArcLight-transfected HEK cells to 0.5-ms electric field pulses of intensities 1, 5 and 10–80 V were recorded on the high-throughput platform. Values represent mean ± s.e.m., n = 24 wells. Responses steadily increased with the intensity of field stimulation at the lower voltages and plateaued between 50 and 60 V. 60 V was chosen as the standard stimulus intensity. (**d**) Software-controlled data acquisition, analysis and storage. Left, acquisition control panel written in LabView. The software allows the user to control microscope hardware, start, stop or resume acquisition and view the current FOV and screening progress. Center, data are extracted using a mask image (top) and time-series plots of fluorescence change are generated for all identified cells in a FOV (bottom). Red trace indicates the maximum fluorescence response. Right, the maximum responses from individual wells are entered into a FileMaker database, which also has information on the plate, libraries and transfection. All raw traces are stored and accessed via centrally located server.
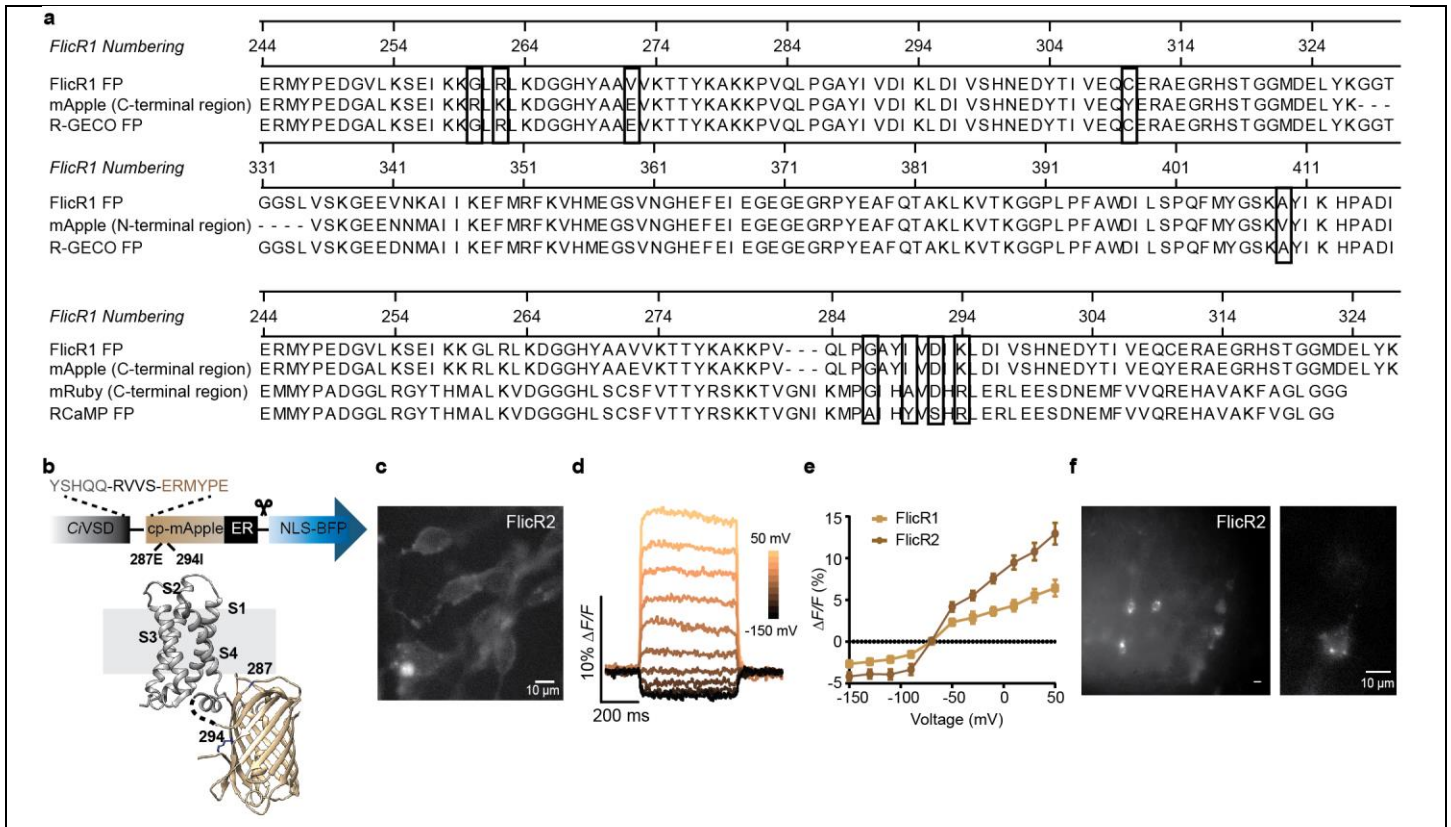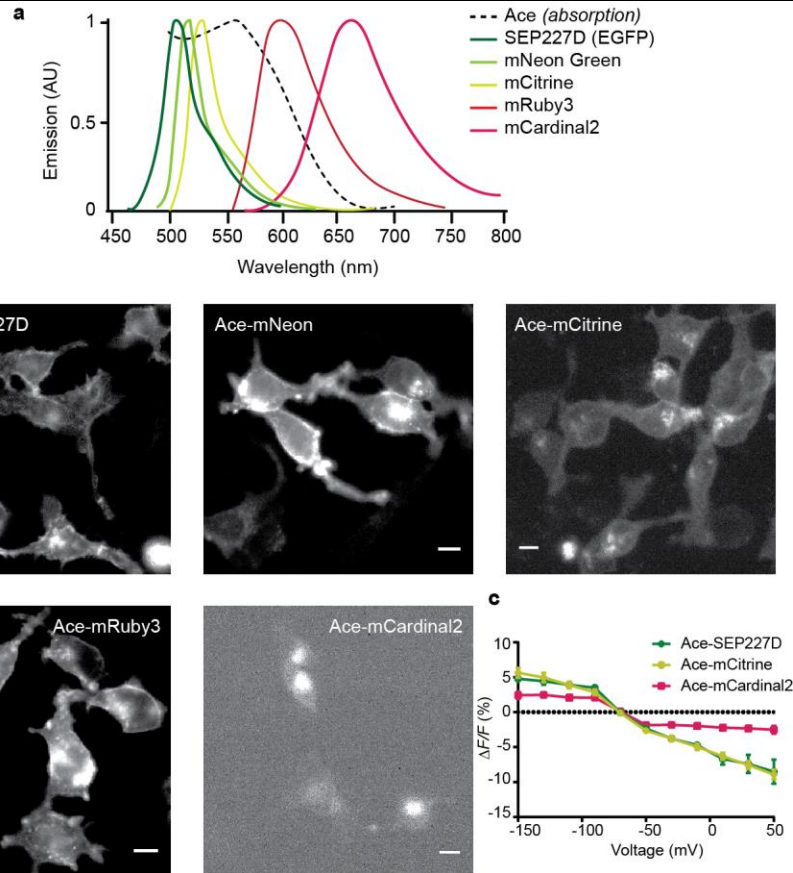
Supplementary Figure 2

Improving the voltage sensitivity of FlicR1 on the screening platform.

(a)   Alignment of amino acid sequence of the FlicR1 fluorophore cp-mApple with mApple sequence[1] and the sequence of R-GECO FP[2], which is a cp-mApple variant. (b) Alignment of amino acid sequences of cp-mApple in FlicR1 with the sequences of mApple, mRuby3 and RCaMP FP[3], which is a cp-mRuby variant. Boxes indicate residues in the FP barrel which were targeted for saturation mutagenesis in FlicR1 based on sequence and/or structural homology with key residues that improved performance of R-GECO or RCaMP[2,3]. (**b**) Top, Schematic of the FlicR2 construct fused to a nuclear localization signal (NLS)-tagged blue fluorescent protein (BFP) reporter. FlicR2 and NLS-BFP were interspersed by a T2A peptide (scissor). Mutations in the FP that improved voltage sensitivity are shown. Bottom, crystal structures of CiVSD (PDB 4G80) and cp-mApple in R-GECO1 (PDB 4I2Y) in a fusion configuration. S1-4 indicate transmembrane helices of the VSD. (**c**) Epifluorescence image of HEK cells expressing FlicR2 ($n = 12$ wells, 3 cultures). (**d**) Fluorescence responses from a FlicR2-transfected HEK cell held at –70 mV to depolarizing and hyperpolarizing voltage steps (Δ20 mV). (**e**) Fluorescence-voltage ($\Delta F/\Delta V$) plots for FlicR1 and FlicR2 in HEK cells ($n = 4$ and 6 cells, respectively). Values represent mean ± s.e.m. (**f**) Epifluorescence images of FlicR2-electroporated pyramidal neurons (left) and magnified images of a soma (right) in an acute brain slice ($n = 8$ neurons).

1.   Shaner, N. C. et al. Improving the photostability of bright monomeric orange and red fluorescent proteins. *Nat. Methods* **5**, 545–551 (2008).

2.   Zhao, Y. et al. An expanded palette of genetically encoded Ca²⁺ indicators. *Science* **333**, 1888–1891 (2011).

3.   Akerboom, J. et al. Genetically encoded calcium indicators for multi-color neural activity imaging and combination with optogenetics. *Front. Mol. Neurosci.* **6**, 2 (2013).
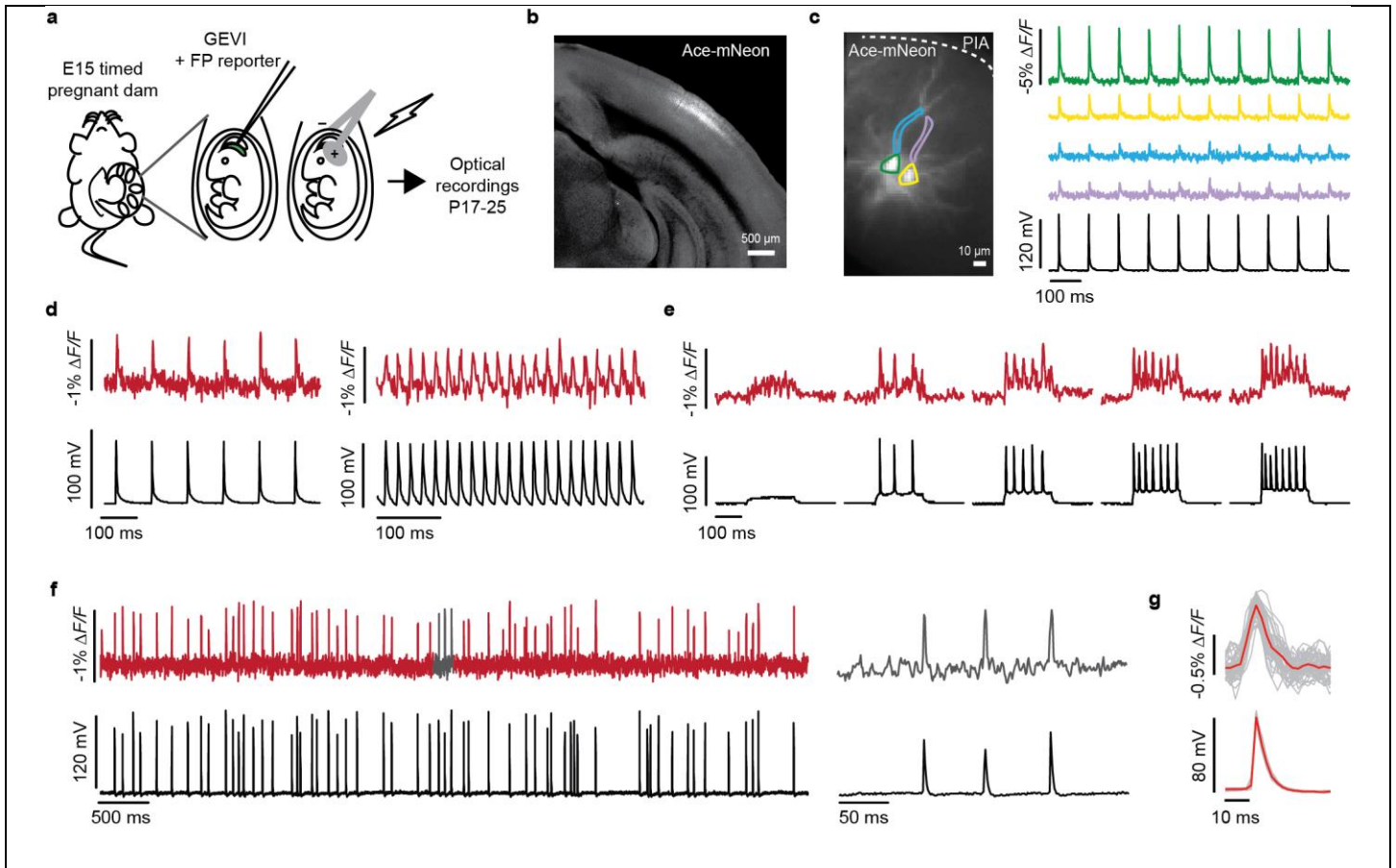
Supplementary Figure 3

Membrane localization and voltage sensitivities of Ace-FP fusions.

(a) Schematic of spectral overlap of the absorption of Ace and emission of indicated fluorophores[4–7]. (b) Epifluorescence images of HEK cells transfected with the Ace-FP fusion constructs. While Ace-SEP227D, Ace-mNeon and Ace-mRuby3 expressed brightly and showed excellent membrane localization, Ace-mCitrine and Ace-mCardinal2 exhibited dim fluorescence and large intracellular aggregates (n = 4 wells per condition, 500 cells per well). (c) $\Delta F/\Delta V$ curves for Ace-mCitrine, Ace-SEP227D and Ace-mCardinal2 in HEK cells acquired during concurrent optical and electrical recordings in voltage clamp (n = 6 cells for Ace-mCitrine and 4 cells each for Ace-SEP227D and Ace-mCardinal2). Values represent mean ± s.e.m. Illumination intensities were 15–20 mW mm^{-2} except for Ace-mCardinal2, which was imaged at 40 mW mm^{-2} at the specimen plane.

4.   Bajar, B. T. et al. Improving brightness and photostability of green and red fluorescent proteins for live cell imaging and FRET reporting. *Sci. Rep.* **6**, 20889 (2016).

5.   Chu, J. et al. Non-invasive intravital imaging of cellular differentiation with a bright red-excitable fluorescent protein. *Nat. Methods* **11**, 572–578 (2014).

6.   Gong, Y. et al. High-speed recording of neural spikes in awake mice and flies with a fluorescent voltage sensor. *Science* **350**, 1361–1366 (2015).

7.   Gong, Y., Wagner, M. J., Zhong Li, J. & Schnitzer, M. J. Imaging neural spiking in brain tissue using FRET-opsin protein voltage sensors. *Nat. Commun.* **5**, 3674 (2014).

Supplementary Figure 4

In utero delivery of GEVI constructs and performance of Ace-mNeon and Ace-mRuby3 in acute, electroporated slices.

(**a**) Schematic of the timeline for in utero electroporation and postnatal optical electrophysiology in acute slices. (**b**) Epifluorescence image of an Ace-mNeon-electroporated slice showing indicator expression in the visual cortex (*n* = 3 mice). (**c**) Left, 80 x 80 pixel CCD image of a pair of pyramidal neurons expressing Ace-mNeon in acute slice. Right, optical and electrical (black) responses from select regions of interest (color-coded) to depolarizing current injections delivered to the green soma via the recording pipette. Large optical signals were observed in the soma, corresponding to APs, while smaller amplitude signals were noted in the blue apical dendrite corresponding to backpropagating APs. Even smaller optical EPSPs were conspicuous in the neighboring yellow cell and its apical dendrite (*n* = 3 experiments). (**d**) Single-trial optical (red) and electrical (black) signals to APs elicited by somatic current injections at 10 Hz (left) and 50 Hz (right). (**e**) Optical and electrical responses to 200-ms somatic current injections of increasing amplitudes (starting at 100 pA, 5 cycles, Δ100 pA). (**f**) Optical recordings of spontaneous APs. Gray spikes are shown at an expanded time scale to the right. (**g**) Mean waveform (red) of the optical and electrical spikes (*n* = 43 spikes). Gray shading represents all spikes combined.

a

Ace | mRuby3 | TS

HETIFK SG L I KENMRMK

HETIFK‒ G L I KENMRMK
HETIFK‒ ‒ L I KENMRMK
HETIFK‒ ‒ ‒ I KENMRMK
HETIFK‒ ‒ ‒ ‒ KENMRMK   **Deletions**
HETIFK‒ ‒ ‒ ‒ ‒ ENMRMK
HETIFK‒ ‒ ‒ ‒ ‒ ‒ NMRMK
HETIFK‒ ‒ ‒ ‒ ‒ ‒ ‒ MRMK

HETIFK X SGL I KENMRMK
HETIFK XX SGL I KENMRMK   **Insertions**
HETIFK XXX SGL I KENMRMK
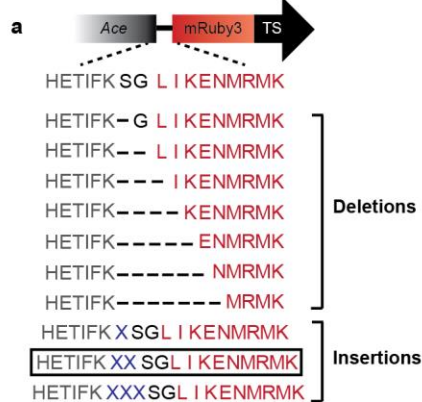
b

	1	2	3	4	5	6	7	8	9	10	11	12
A	0.58	0.88	0.75	0.67	0.63	0.79	0.67	1.04	0.67	0.58	0.71	1.00 Control
B	0.92	0.75	1.08	0.79	0.92	0.17	1.04	1.08	0.46	1.17	0.75	0.71
C	0.46	1.00	1.25 Ile/Phe	0.25	1.21 Ala/Arg	1.08	0.92	1.33	1.04	0.83	0.92	0.50
D	0.67	1.04	1.25 Gly/Gln	1.17 Arg/Gly	1.08 His/Val	1.21	1.29 Leu/Arg	1.04	1.25 Met/His	0.79	0.25	0.83
E	0.96	1.17	1.17	1.17	1.25 Gln/Gly	1.29 Glu/Trp	1.29 Gly/Arg	1.21 Lys/Arg	0.46	1.08	1.17	0.17
F	0.00	1.21	1.08	1.13	1.13	0.92	1.38 Trp/Arg	1.29 Lys/Lys	1.29 Phe/Val	0.88	1.25 Phe/Tyr	0.42
G	0.00	1.04	0.88	1.33 Arg/Arg	0.58	1.25	1.00	0.50	1.04	0.88	0.92	0.67
H	1.08	0.63	0.00	0.38	0.58	0.67	0.58	0.75	0.63	0.75	0.33	1.00 Control

Supplementary Figure 5

Platform-based screening of linker mutations in Ace-mRuby3.

(**a**) Schematic of deletional and insertional mutations in the Ace-mRuby3 linker. Residues in the linker and N-terminus of the FP (unstructured region) were sequentially deleted to bring mRuby3 closer to Ace. Single, double or triple AA insertions were achieved by introducing one, two or three NNK codons, respectively. Of all 288 variants screened on the platform, only the double AA insertions showed improvements in voltage sensitivity. (**b**) Screening results obtained on the platform for the double insertion library (96 variants). Fluorescence responses in individual wells are indicated. Responses are normalized to control (Ace-mRuby3, wells A12 and H12). Red and blue wells represent variants that performed better or worse than control, respectively. Some of the top performing wells were sequenced. The best performing well F7 contained a tryptophan/arginine insertion. 7 of 17 sequenced wells (41%) had at least one arginine insertion.
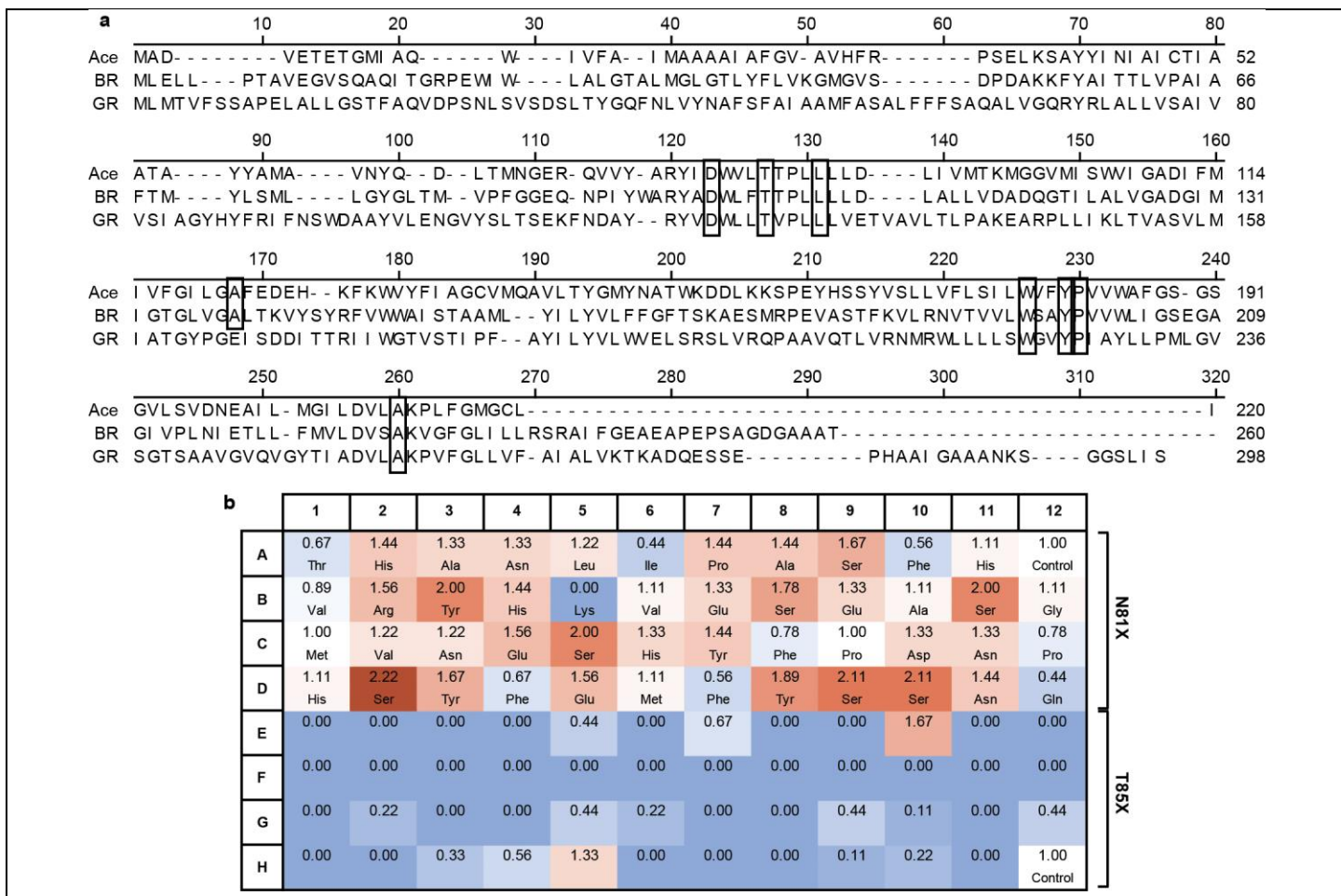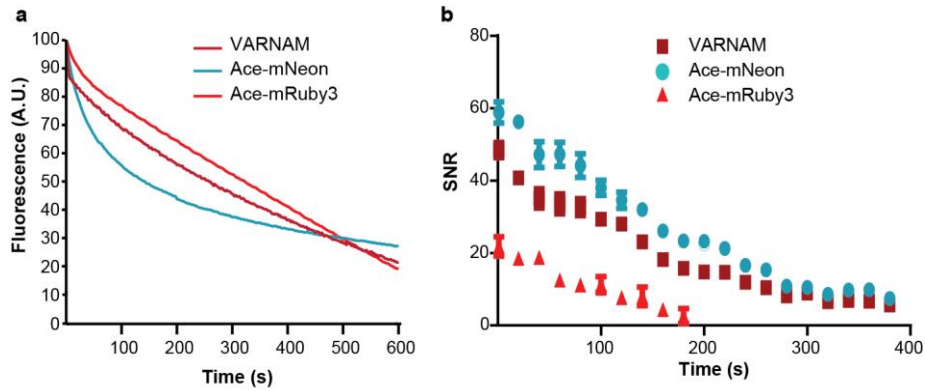
Supplementary Figure 6

High-throughput voltage screening of Ace-mRuby3 RBP mutants.

(**a**) Alignment of amino acid sequences of Ace, bacteriorhodopsin (BR) and *Gloeobacter* rhodopsin (GR). Boxes indicate conserved residues constituting the RBP, mutations of which have been shown to modulate the opsin's absorption spectrum in BR and GR[8–10]. The corresponding sites in Ace were targeted for saturation mutagenesis in Ace-mRuby3 and again in Ace-WR-mRuby3. (**b**) Screening results on the platform for the Ace-WR-mRuby3 N81X library, which was part of a 96-well plate that also contained the Ace-WR-mRuby3 T85X library. Fluorescence responses in individual wells are indicated. Responses are normalized to control (Ace-mRuby3, wells A12 and H12). Red and blue wells represent variants that performed better or worse than control, respectively. The wells indicate individual mutations. N81S, which was represented seven times in the plate, was on average twice as sensitive as control in quadruplicate screens. Contrary to N81X, T85X was mostly detrimental to voltage sensitivity.

8.   Engqvist, M. K. et al. Directed evolution of *Gloeobacter violaceus* rhodopsin spectral properties. *J. Mol. Biol.* **427**, 205–220 (2015).

9.   Greenhalgh, D. A., Farrens, D. L., Subramaniam, S. & Khorana, H. G. Hydrophobic amino acids in the retinal-binding pocket of bacteriorhodopsin. *J. Biol. Chem.* **268**, 20305–20311 (1993).

10.   Russell, T. S., Coleman, M., Rath, P., Nilsson, A. & Rothschild, K. J. Threonine-89 participates in the active site of bacteriorhodopsin: evidence for a role in color regulation and Schiff base proton transfer. *Biochemistry* **36**, 7490–7497 (1997).

Supplementary Figure 7

Photobleaching characteristics of VARNAM.

(**a**) Photobleaching curves of VARNAM, Ace-mNeon and Ace-mRuby3 in HEK cells under continuous illumination (n = 9, 7 and 9 cells, respectively). Imaging conditions: 565-nm LED (VARNAM and Ace-mRuby3) and 505-nm LED (Ace-mNeon); 15 mW mm^{-2}. Photobleaching time constants were 256 s for VARNAM, 304 s for Ace-mRuby3 and 142 s for Ace-mNeon. (**b**) SNR at photobleaching rates in cultured cells under continuous illumination as above. Optical responses to Δ120 mV/5 Hz voltage steps were acquired for 1 s after every 19 s and averaged across multiple cells. The noise was determined as the s.d. of baseline fluorescence during a 100-ms interval preceding the first spike in every time bin. Values represent mean ± s.e.m. n = 6 cells per condition.
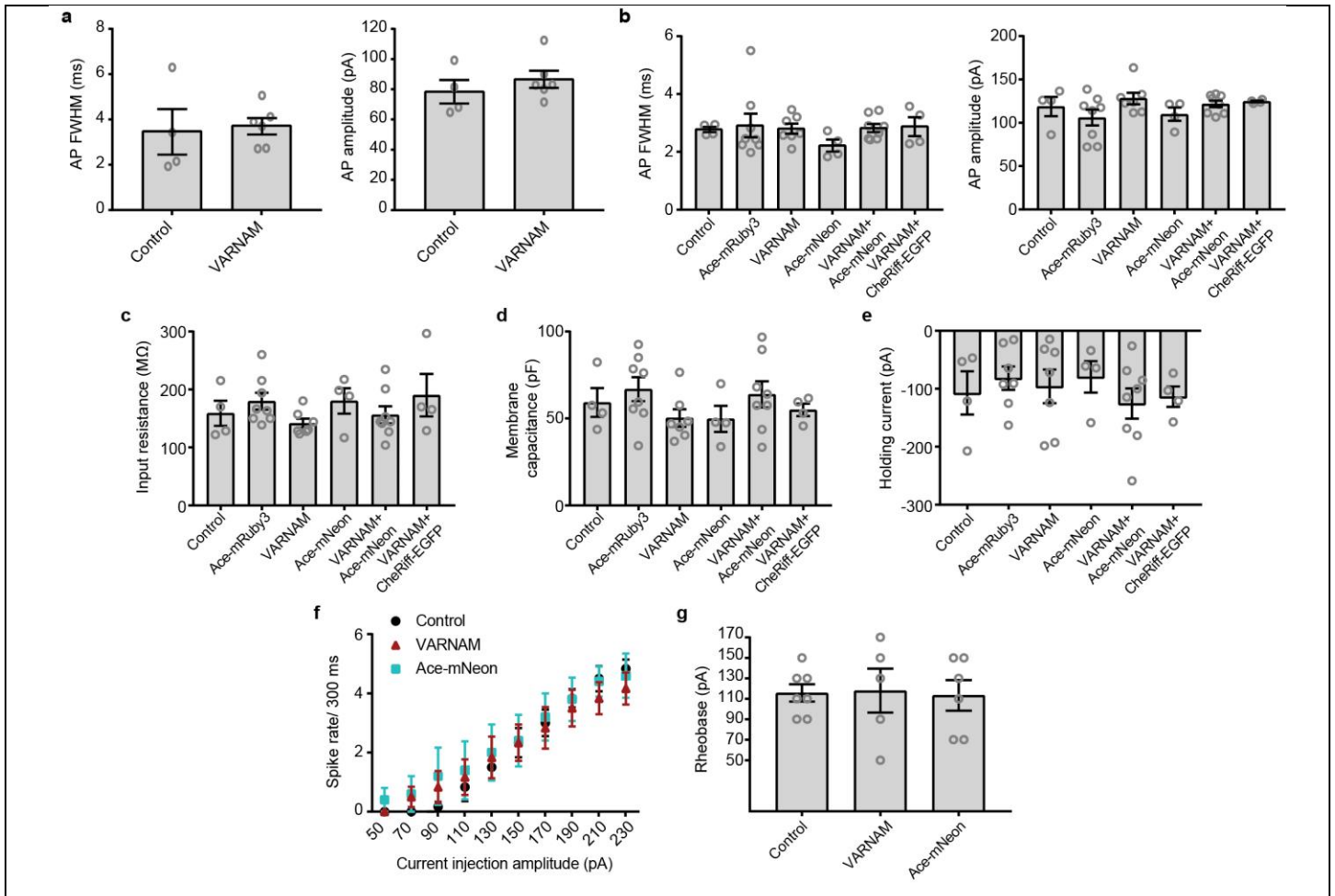
Supplementary Figure 8

Passive membrane properties and intrinsic excitabilities of control and indicator-expressing neurons.

(**a**) AP FWHM and amplitude in GFP and VARNAM-transfected primary neurons. $P = 0.47$ and $P = 0.35$, respectively, two-tailed Mann–Whitney U test; $n = 4$ neurons (control), 6 neurons (VARNAM). (**b**) FWHM and amplitudes of spike waveforms from neurons electroporated with indicated constructs and control cells in acute brain slices. $P > 0.99$, Kruskal–Wallis test with Dunn's multiple comparisons correction; $n = 4$ neurons per condition (control, Ace-mNeon and VARNAM+CheRiff-EGFP), 7 neurons (VARNAM) and 8 neurons per condition (Ace-mRuby3 and VARNAM+Ace-mNeon). (**c**) Input resistance, (**d**) membrane capacitance and (**e**) holding current ($V_H = -65$ mV) values of neurons electroporated with indicated constructs and control cells in acute slices. $P > 0.99$, Kruskal–Wallis test with Dunn's multiple comparisons correction; $n = 4$ neurons per condition (control, Ace-mNeon and VARNAM+CheRiff-EGFP), 7 neurons (VARNAM) and 8 neurons per condition (Ace-mRuby3 and VARNAM+Ace-mNeon). (**f**) Mean ± s.e.m. spike rate during a 300-ms epoch plotted as a function of the amplitude of current injection for control, VARNAM and Ace-mNeon-electroporated neurons. (**g**) Rheobase values of control, VARNAM and Ace-mNeon-neurons in (**f**). $P > 0.99$, Kruskal–Wallis test with Dunn's multiple comparisons correction; $n = 7$, 5 and 6 neurons for control, VARNAM and Ace-mNeon conditions, respectively. (**a-e**), (**g**), Values represent mean ± s.e.m.
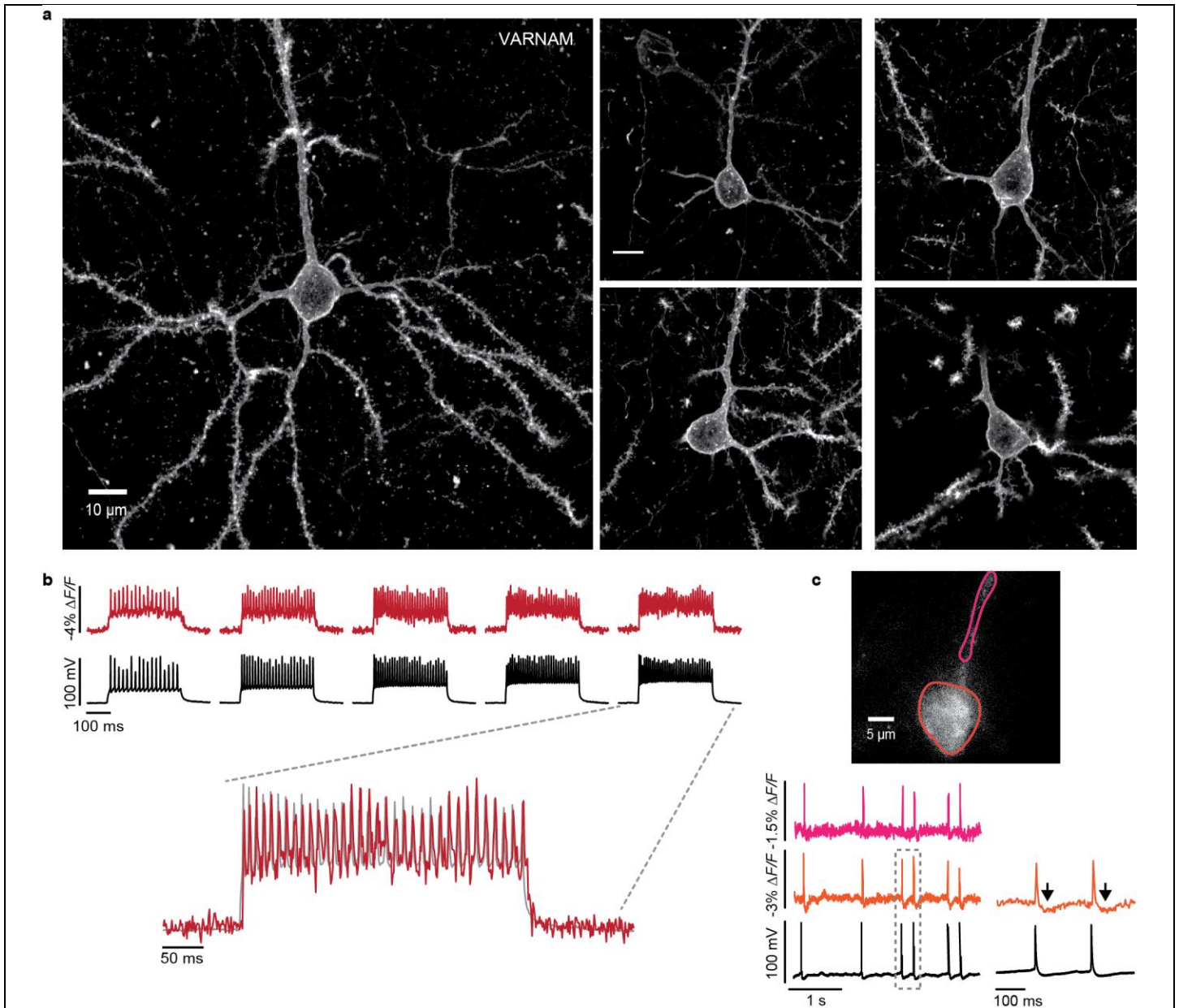
Supplementary Figure 9

**VARNAM expression in electroporated neurons and optical recordings in acute slices.**

(**a**) High-resolution confocal images of VARNAM-expressing superficial layer pyramidal neurons in fixed brain slice. Vivid membrane localization with minimal intracellular aggregation was noted. (**b**) Concurrent optical (red) and electrical (black) recordings of high-speed AP bursts in a VARNAM-expressing neuron in acute brain slice. Bursts were triggered by current injections of 300-ms duration at increasing amplitudes (starting at 200 pA, 5 cycles, Δ100 pA). Dashed lines indicate trial shown at an expanded time scale below, overlaid with the optical trace. (**c**) Concurrent optical and electrical recordings of spontaneous APs in a VARNAM-expressing neuron in acute brain slice. Optical APs were observed in the soma (orange) and proximal apical dendrite (pink). Dashed box indicates time frame expanded to the right. Arrows indicate afterhyperpolarizations recapitulated in the optical trace.
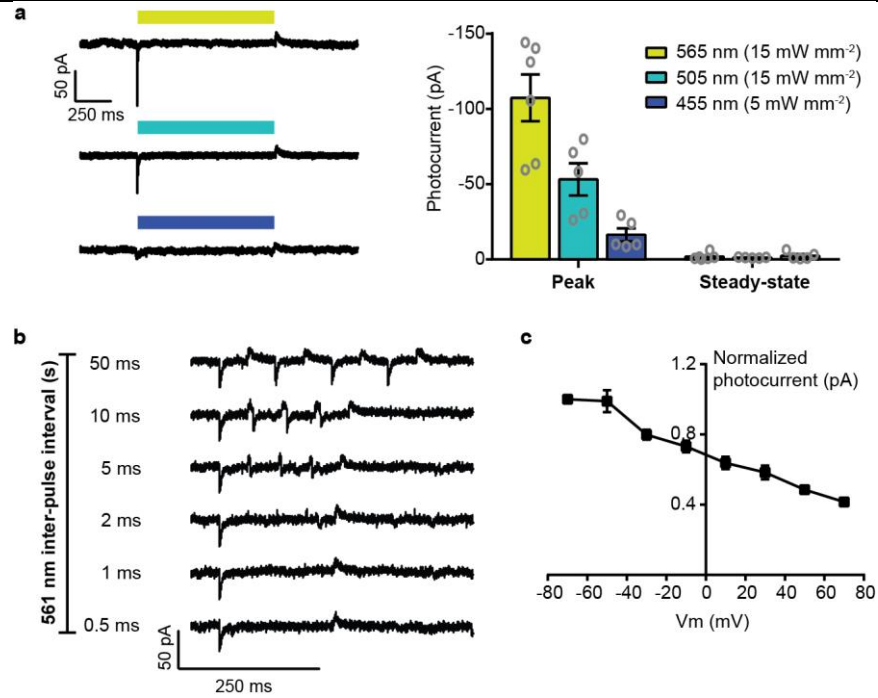
Supplementary Figure 10

VARNAM-positive neurons exhibit negligible steady-state photocurrents.

(**a**) Left, representative electrical recordings of photocurrents in VARNAM-positive neurons during a 1-s illumination with wavelengths of 565, 505 and 450 nm in acute slice. Right, mean peak and steady-state photocurrents at the different wavelengths. Error bars represent s.e.m. Neurons exhibited peak photocurrents of 107.4 ± 15.5, 53.24 ± 10.73 and 16.41 ± 4.3 pA and steady-state currents of 1.86 ± 0.9, 1.24 ± 0.14 and 2.4 ± 1.0 pA under 565-nm, 505-nm and 450-nm light, respectively. n = 6, 5 and 5 neurons, respectively. The latter was computed by subtracting the average current across the last 10 ms of illumination from the mean current preceding light onset. (**b**) To compute the refractory period of the transient photocurrent, we modulated the frequencies of 50-ms-long 561-nm light pulses, as indicated. The currents began to disappear at interpulse intervals of 2 ms and were undetected at higher frequencies. This refractory period is well above the laser modulation frequencies used in TEMPO recordings (>5 kHz). (**c**) To determine the reversal potential of the current, we voltage-clamped HEK cells and measured the peak photocurrent during 1 s of illumination with 561-nm light at indicated V_H. The current did not dissipate in the physiological range of depolarizing potentials but exhibited progressively smaller amplitudes. n = 5 cells. Values represent mean ± s.e.m.
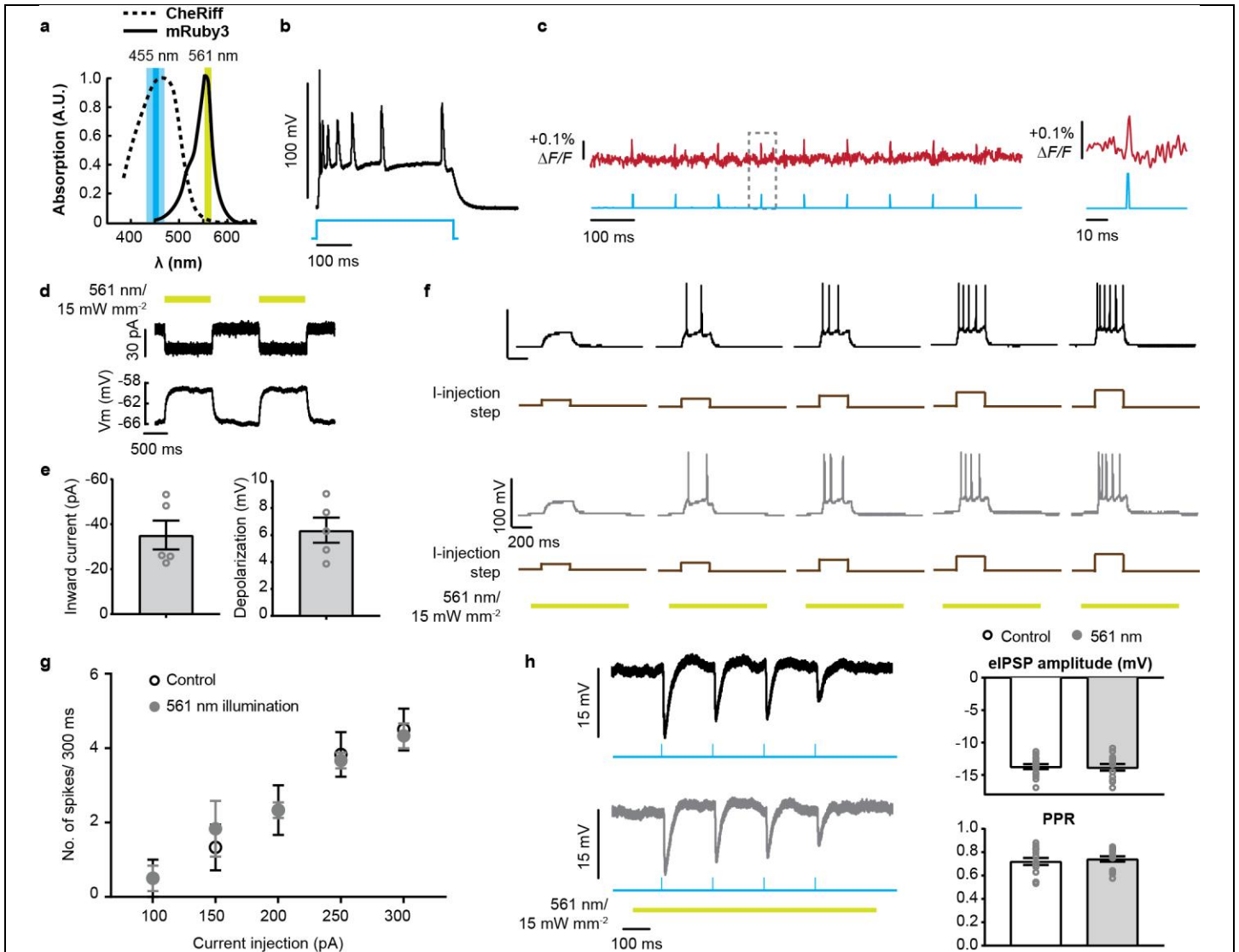
Supplementary Figure 11

**Optical cross-talk in all-optical experiments with VARNAM in acute slices.**

(**a**) Overlay of the action spectrum of CheRiff and excitation spectrum of mRuby3. Blue and green lines denote wavelengths used for excitation of CheRiff and VARNAM, respectively. (**b**) Burst firing in CheRiff-expressing neurons in acute slice during 300 ms of blue light stimulation (455-nm LED, 2.4 mW mm^{-2}). (**c**) Blue-light artifact in VARNAM-positive but CheRiff-negative neurons during 0.5-ms light pulses (455-nm LED, 2.4 mW mm^{-2}). Gray shaded box denotes interval shown at an expanded time scale. Note the polarity, kinetics and size of the transient, which are distinct from voltage signals. (**d**) Representative electrical recordings in voltage clamp (top) and current clamp (bottom) showing depolarization induced in CheRiff-electroporated neurons during 561-nm illumination. Yellow lines indicate illuminated time intervals. (**e**) 561-nm light generated an average inward current of 35.21 ± 6.4 pA (left) resulting in an average voltage depolarization of 6.4 ± 0.9 mV (right). n = 5 neurons from 2 mice. (**f**) AP bursts induced in CheRiff-positive neurons by 300-ms current injections of increasing amplitudes (starting at 100 pA, 5 cycles, Δ50 pA) in the absence (top) and presence (bottom) of 1-s illumination with 561-nm light. (**g**) Average spike rate in the control and illuminated conditions plotted as a function of the amplitude of current injection (n = 6 neurons from 3 mice). (**h**) Optical cross-talk in cell-type-specific all-optical recordings in PV-Cre[+] mice. Left, representative eIPSPs induced by blue light pulses in the absence (top) and presence (bottom) of 561-nm light. Vertical blue lines indicate incidence of 455-nm light (2 mW mm^{-2}). Right, quantifications of the amplitude of the first eIPSP (top) and paired-pulse ratios (PPR) (bottom) during optogenetic activation in the absence and presence of 561-nm light. n = 14 trials from the same cell, epochs without and with 561-nm illumination were interleaved, P = 0.8 and 0.6, respectively, two-sided Wilcoxon test. (**e**), (**g**), (**h**), Values represent mean ± s.e.m.
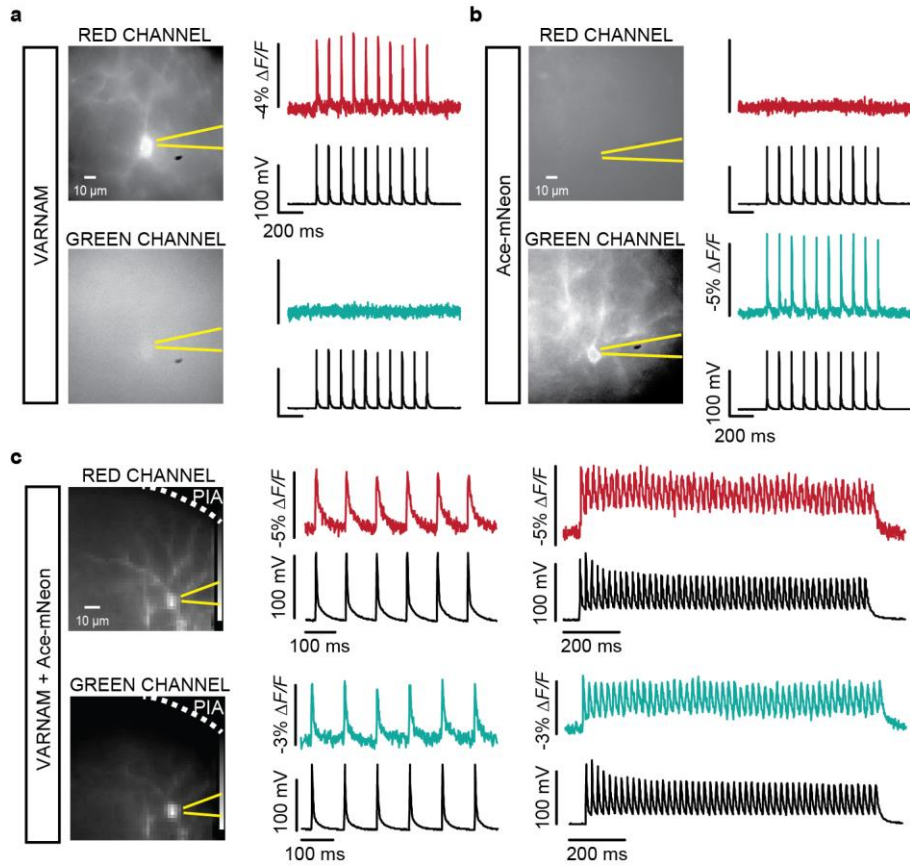
Supplementary Figure 12

Dual-color voltage imaging in acute slices.

(**a-c**) Left, 80 x 80 pixel image of a neuron in slice electroporated with (**a**) VARNAM, (**b**) Ace-mNeon and (**c**) VARNAM and Ace-mNeon imaged in the red and green channels. Recording pipette is shown in yellow. (**a-b**) Right, optical (colored) and electrical (black) recordings of 10-Hz current-induced APs, sequentially recorded in the two channels. (**c**) Optical (colored) and electrical (black) recordings of 10-Hz (center) or 50-Hz (right) current-induced APs, sequentially recorded in the two channels. Illumination: 561-nm laser (VARNAM), 488-nm laser (Ace-mNeon), 15 mW mm^{-2}.
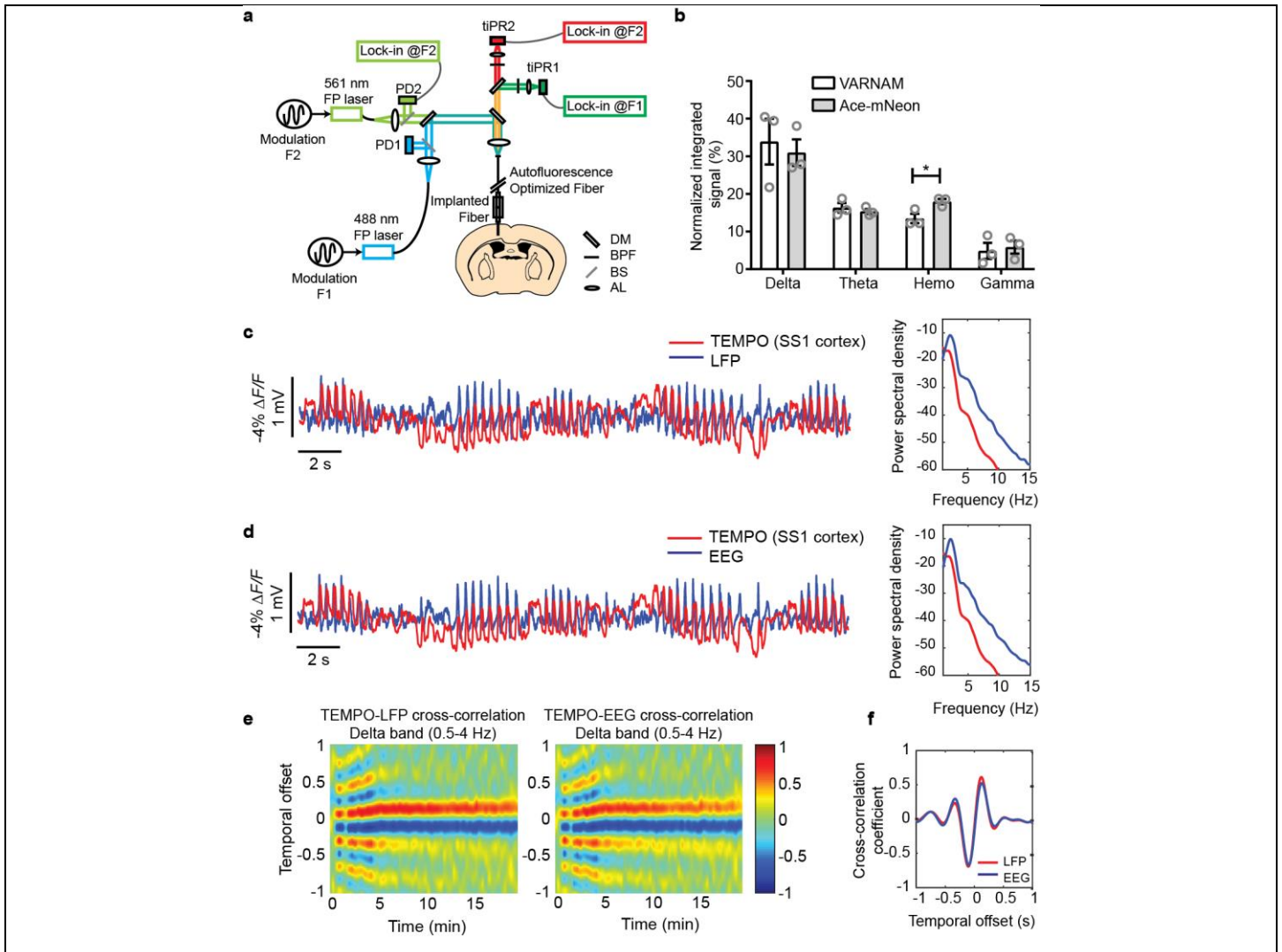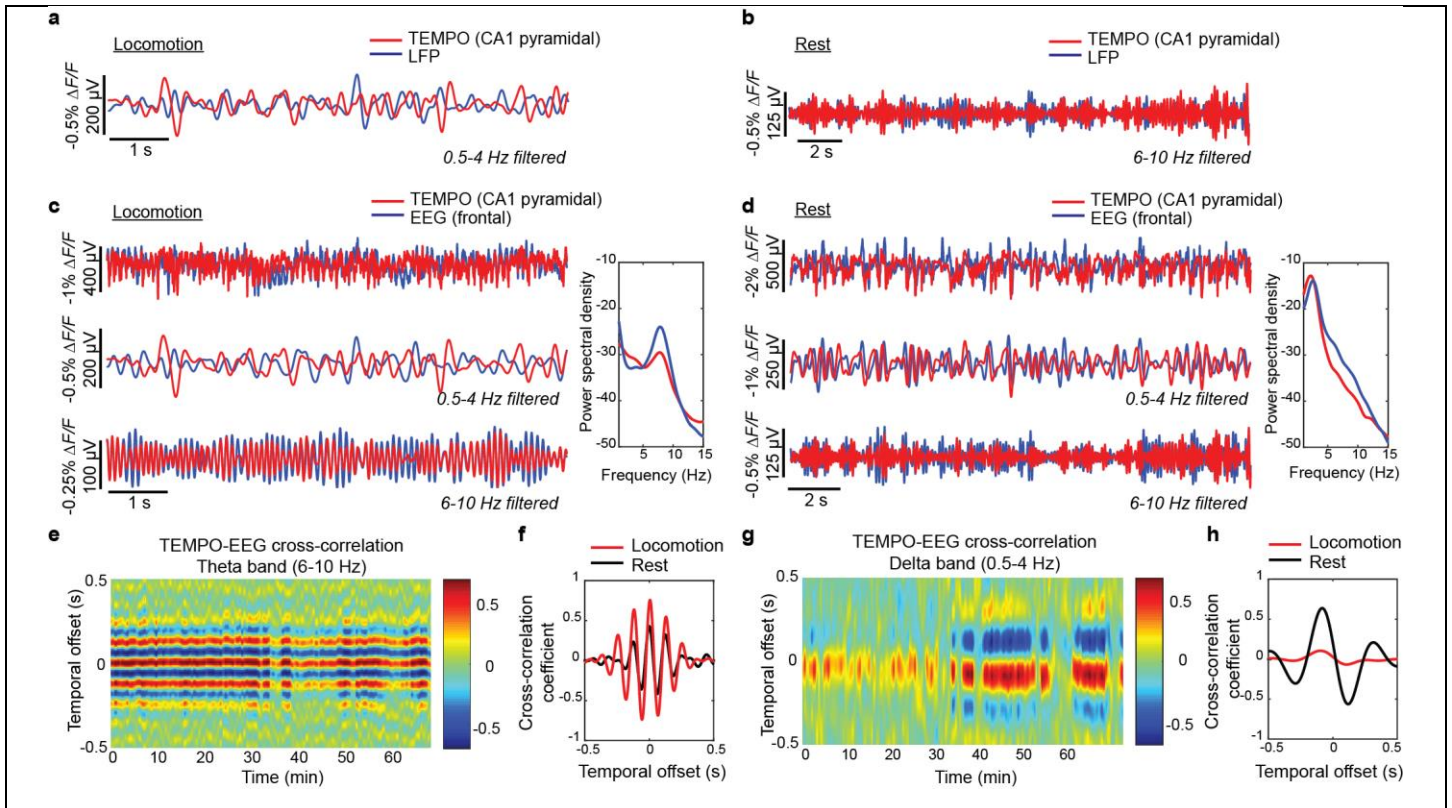
Supplementary Figure 13

VARNAM reports oscillatory dynamics in cortical pyramidal neurons in anesthetized mice.

(**a**) Optical sketch of the TEMPO apparatus for VARNAM recordings. Two single-mode fiber pigtailed lasers emitting at 488 nm and 561 nm were used for the green reference channel (YFP) and the red voltage channel (VARNAM), respectively. Photodiodes monitored the fluctuations in the beams' intensities. Only the 561-nm laser showed prominent fluctuations that impeded the red voltage channel recording. This signal was systematically extracted to unmix the red signal. The beams were combined and focused onto a polymer-clad multi-mode optical fiber, which delivered light to the brain via implanted fiber. Fluorescence was collected via the same fiber, split into green and red emissions, and detected by transimpedance photoreceivers. (FP: fiber pigtailed; PD: photo detector; tiPR: transimpedance photoreceiver; DM: dichroic mirror; BPF: band-pass filter; BS: beam splitter; AL: astigmatic lens). (**b**) Normalized integrated signal in the indicated frequency bands in VARNAM and Ace-mNeon recordings. The hemodynamic frequency band (11-14 Hz) showed significantly reduced normalized integrated signal in VARNAM recordings compared to Ace-mNeon, suggesting that VARNAM may provide a better SNR in the biologically-relevant theta band (13.5 ± 1% (VARNAM) versus 18 ± 0.5% (Ace-mNeon), mean ± s.e.m., *P = 0.034, two-tailed t-test, n = 3 mice per condition). The integrated power was comparable between the indicators in the delta (1-4 Hz), theta (6-10 Hz) and gamma bands (25-50 Hz). (**c-d**) Left, unfiltered time traces of TEMPO and (**c**) LFP or (**d**) EEG during anesthesia, showing closely matched oscillations. Right, normalized power spectral density. Note the prominent delta rhythm in both cases (0.5 Hz-4 Hz). (**e**) To assess the coherence of TEMPO and LFP (right) or EEG (left) oscillations, we computed the cross-correlation in 10-s increments across a 20-min recording just after KX injection. Consistent slow wave synchrony appeared a few tens of seconds after KX injection and reached steady-state in <5 min. (**f**) Average cross-correlation coefficient in the delta band.

Supplementary Figure 14

VARNAM reports state-dependent voltage oscillations in a freely behaving mouse.

(**a-b**) Time traces of TEMPO and LFP during (**a**) locomotion and (**b**) rest. Traces showed low-matched oscillations during both states in the opposite band (delta and theta band, respectively). (**c-d**) Left, time traces of TEMPO and EEG during (**c**) locomotion and (**d**) rest showing raw, delta-band-filtered and theta-band-filtered traces. Right, normalized power spectral density. Note the prominent theta rhythm (6 Hz-10 Hz) during locomotion and delta rhythm (0.5 Hz-4 Hz) at rest. (**e, g**) Cross-correlation plot between TEMPO and EEG filtered in the (**e**) theta and (**g**) delta bands. Two-state behavior is evident with high coherence in the theta band during locomotion (beginning of recording) and delta band at rest (end of recording). (**f, h**) Average cross-correlation coefficient in the (**f**) theta and (**h**) delta bands during locomotion and rest, showing opposite frequency band content.
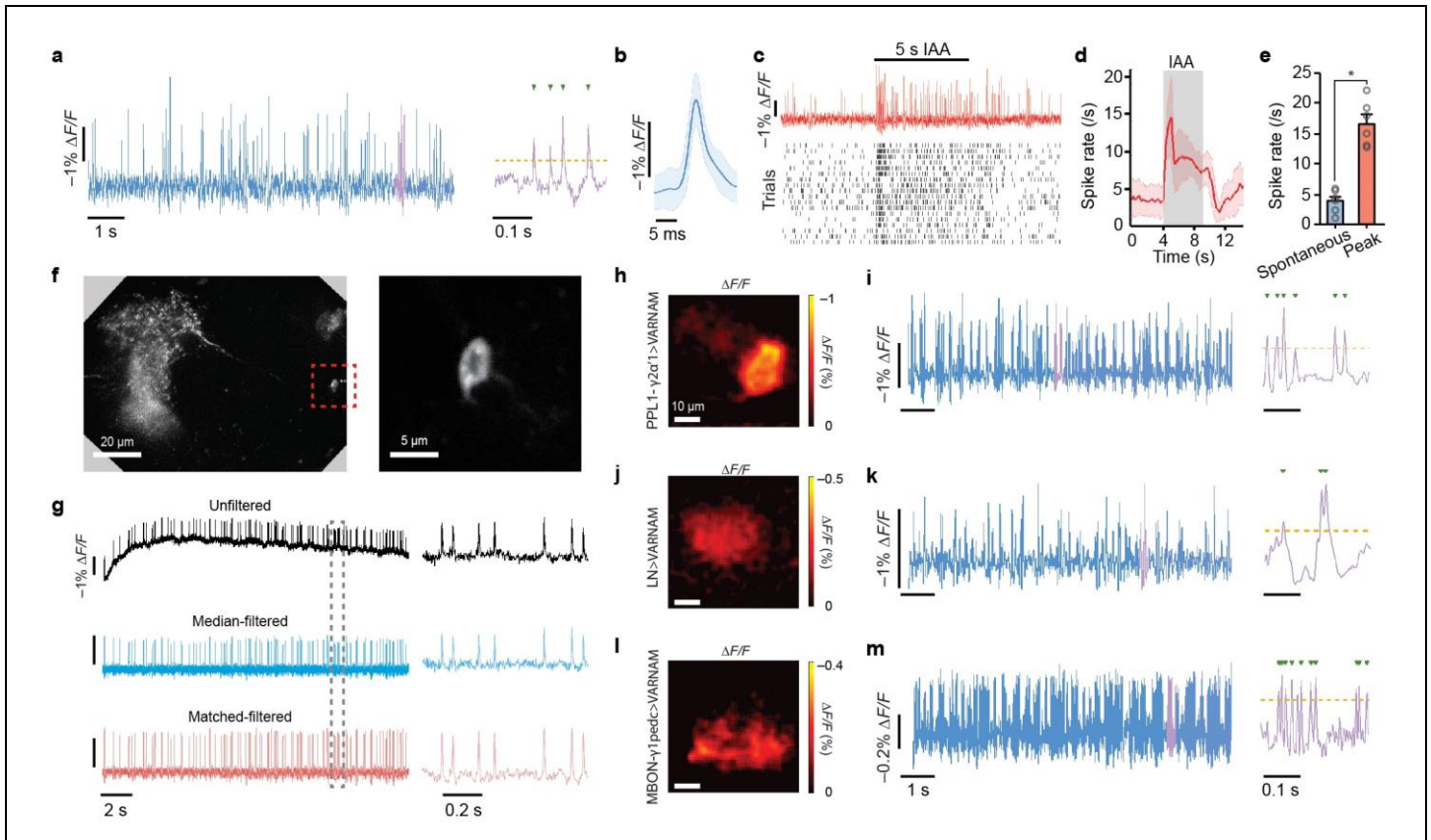
Supplementary Figure 15

Imaging spontaneous and odor-evoked spiking in live *Drosophila*.

(**a**) Optical voltage trace acquired from *MB058B-GAL4>20xUAS-Ace2N-2AA-mNeon* fly, showing spontaneous spiking in a PPL1-α'2α2 neuron over 10 s (left), and a 0.3-s interval shown at expanded time scale (right). Yellow dashes indicate spike detection threshold. Green arrows denote identified spikes. (**b**) Mean spike waveform (blue trace) from recordings in (**a**) (n = 172 spikes). Blue shading denotes s.d. (**c**) Top, example trace of evoked spiking in PPL1-α'2α2 during 5-s IAA presentation. Bottom, raster plots of 18 trials of odor-evoked spiking (n = 6 flies). (**d**) Time-varying mean spike rates computed from recordings in (**c**). Red shading denotes s.d. (**e**) Mean peak spike rate before and during odor presentation. Error bars represent s.e.m. *P = 0.03, two-sided Wilcoxon signed-rank test, n = 6 flies. (**f**) Two-photon image showing axonal region and soma of a PPL1-α'2α2 neuron in a *MB058B-GAL4>20xUAS-VARNAM* fly (left). Red dotted box denotes region magnified (right), showing VARNAM localization on the membrane. (**g**) Matched-filtering algorithm used in voltage imaging analysis in Fig. **6** (**c**), (**e**) and (**i**). Optical voltage trace showing spontaneous spiking in PPL1-α'2α2 over 20 s (left), and a 1-s interval shown at expanded time scale (right). Top to bottom, representative unfiltered, median-filtered and matched-filtered traces. (**h-m**) Imaging spontaneous spiking in three neuron types using VARNAM (n = 6 flies per condition). (**a**), (**c**) and (**e**) Spatial map of *ΔF/F* during spiking in (**a**) the axonal region of PPL1-γ2α'1 in a *MB296B-GAL4>20xUAS-VARNAM* fly, (**c**) the dendritic tree of MBON-γ1pedc in a *MB085C-GAL4>20xUAS-VARNAM* fly, and (**e**) the dendritic tree of olfactory LN in a *R55D11-GAL4>20xUAS-VARNAM* fly. (**b**), (**d**) and (**f**) Optical voltage traces of spontaneous spiking in (**a**), (**c**) and (**e**), respectively, over 10 s (left), and a 0.3-s interval shown at expanded time scale (right). Yellow dashed line indicates spike detection threshold. Green arrows denote identified spikes.

Supplementary Table

GEVI	Rise time		Decay time	
	τ_{fast} (ms)	τ_{slow} (ms)	τ_{fast} (ms)	τ_{slow} (ms)
FlicR1	3.2 ± 0.2	31.5 ± 3.8	2.6 ± 0.3	25.8 ± 1.5
FlicR2	2.9 ± 0.2	29.5 ± 2.1	3.1 ± 0.6	28.5 ± 4.5
Ace-mRuby3	0.99 ± 0.03	5.5 ± 0.4	0.93 ± 0.2	5.1 ± 0.7
VARNAM	0.88 ± 0.13	5.2 ± 0.5	0.80 ± 0.44	4.7 ± 0.3
Ace-mNeon	0.81 ± 0.14	4.6 ± 0.3	0.77 ± 0.19	5.2 ± 0.5

Fluorescence response kinetics of VARNAM, FlicR and Ace-mNeon. Responses to depolarizing voltage steps in HEK cells were fitted using a biexponential step function to determine rise and decay kinetics. τ_{fast} and τ_{slow} indicate time constants of the fast and slow components, respectively. Imaging conditions: 561 nm laser, 50 mW mm^{-2} for FlicR1/2; 565 nm LED, 15 mW mm^{-2} for VARNAM and Ace-mRuby3 and 505 nm LED, 15 mW mm^{-2} for Ace-mNeon; image acquisition: 3-5 kHz. n=3 cells each (FlicR1, Ace-mRuby3, Ace-mNeon); 4 cells each (FlicR2 and VARNAM). Values represent mean ± S.E.M.

Supplementary Notes

Supplementary Note 1

High-throughput semi-automated screening of voltage indicators. Our voltage screening methodology comprised high-throughput generation of mutagenic GEVI libraries, followed by semi-automated functional screening of transfected cells on a custom platform, equipped with an epifluorescence microscope.

Library generation and transfection. For high-throughput site-directed saturation mutagenesis, we used partially-overlapping primers for mutagenizing-polymerase chain reactions (PCR).

A set of four forward primers, each consisting of one of four degenerate codons WKC, NMC, VWG or DGG at the target site, were designed to represent all 20 amino acids (AAs) at least once. The target site in the primers was flanked on either end by ~15 NTs. A single reverse primer was designed to partially overlap with the forward primers to facilitate ligation. Mutagenizing PCR was set up using CloneAmp^{TM} polymerase (Clontech). Unmutated template was removed by DpnI treatment, and linear products were circularized using InFusion$^®$ ligase (Clontech) and transformed in TOP10 competent cells (Invitrogen). To obtain up to 19 unique AA substitutions at a single target site, 48 colonies were picked and cultured in 96 deep-well culture plates.

Mutagenesis using the above protocol was substantially more efficient compared to conventional methods using fully complementary primers (QuikChange kit, Agilent) or fully non-overlapping primers (Q5$^®$ site-directed mutagenesis kit, NEB). A significant number of mutants generated using the latter protocols had tandem primer insertions or deletions at the target site (15% of all mutants in the QuikChange reactions (n=7 libraries) and 23% in the Q5$^®$ reactions (n=5 libraries) compared to 0% in our protocol). We also found an overrepresentation of the wildtype variant (17% in the QuikChange reactions and 30% in the Q5$^®$ reactions). Although we initially ascribed this problem to incomplete removal of unmutated template, we found that it was not due to inadequate DpnI activity but in fact due to inefficient plasmid circularization at the final step. The presence of complementary overhangs at the ends of the DNA and the inclusion of a ligase to our protocol improved circularization of PCR-synthesized mutant molecules increasing their representation in the clones.

Plasmid DNA were purified in a high-throughput format using Nucleospin® 96 Plasmid kit (Macherey-Nagel) on an epMotion 5075 liquid handling workstation (Eppendorf). The purified DNA were collected in 96-well plates. Each plate consisted of one or two independent libraries (library=a set of 96 or 48 clones harboring point mutations at a given target site). The libraries were routinely sent for DNA sequencing to identify the individual mutations, ensure plasmid DNA integrity and adequate coverage (>18) of individual AAs.

Excitable HEK cells (ATCC® CRL-3269^{TM}) [11] were maintained in DMEM/F12, 10% FBS, 1% penicillin (100 U ml^{-1}), streptomycin (100 µg ml^{-1}), geneticin (500 µg ml^{-1}), and puromycin (2 µg ml^{-1}). Cells were plated on 96-well glass-bottomed plates, in antibiotic-free media, ~24 h prior to transfection. Plates were transfected with mutagenic GEVI libraries (0.2 µg/well of plasmid DNA using Lipofectamine®) and imaged 24-48 h after transfection. One library typically consisted of 48 clones mutated at a single target residue. Each 96-well plate typically contained two independent libraries.

Semi-automated platform system components. The high-throughput fluorescence imaging platform is built around a Nikon Ti Eclipse inverted microscope fitted with a Nikon Plan Apo 20x 0.75 NA air objective lens, a Perfect Focus System and a motorized filter turret. We designed an innovative 32 x 20 x 3 cm imaging unit which consists of three parts – base, top and electrode assembly. The base of the unit is fixed to the movable XY stage of the microscope and contains a 12.7 x 8.6 cm slot in the center to hold the specimen plate. A moat around the slot holds water to maintain humidity, and heating resistors under the base maintain feedback-controlled temperature at 37˚C during an imaging session. The top of the unit contains a detachable 16.5 x 12.7 cm lid carved out of the center. The electrode housing, with its center aligned to the light path, is attached to the lid. The electrode assembly consists of 0.5 mm diameter platinum wires threaded through holes in a two-pronged electrode holder controlled by an actuator. The top itself is anchored to an anti-vibration table, on which the microscope is seated, via four metal posts. An air gap of 1 mm separates the top from the base to reduce excessive load on the XY stage from friction contact.

Optical setup. A white light source pE-300 (CoolLED, UK) is used for sample illumination. For imaging ArcLight and Ace-mNeon, we use a 472/30 nm excitation filter, 495 nm dichroic mirror and 520/35 nm emission filter (Semrock). For FlicR, VARNAM and mCherry (reporter), we use a 560/40 nm excitation filter, 585 nm dichroic mirror and 630/75 nm emission filter (Chroma Technologies Corporation). The BFP and mCerulean reporters in the FlicR and Ace-mRuby3 constructs are imaged using a 402/20 nm excitation filter, 430 nm dichroic mirror and 460/50 nm emission filter (Semrock) and 455/40 nm excitation filter, 458 nm dichroic mirror and 480/30 nm

emission filter (Semrock), respectively. The trigger for the light source is delivered via a data acquisition board (USB-6008, National Instruments). High resolution images are collected using ORCA Flash4.0 sCMOS camera (Hamamatsu) at 50 Hz.

Image acquisition. Movements of the XY stage, the stimulation electrode, the light source and the camera are controlled using a custom virtual instrument written in LabView® (National Instruments). When a sample plate is placed in the imaging unit, the lid is secured in place and the assay sequence started. The software moves the XY stage to align the predetermined center of well A1 along the light path and the actuator lowers the electrode into the well. An automated filter turret places the appropriate filter cube in the light path. Once inside well A1, the electrode assembly moves in tow with the stage to acquire images from different fields of view (FOVs). A cell searching algorithm collects images from sixteen FOVs in a 4 x 4 grid. The FOVs are ranked in terms of the number of transfected cells. The top four FOVs are revisited, the light source turned ON and high-resolution time-series fluorescence images (700 x 700 µm, 2048 x 2048 pixels) are collected for 5 s either in the stimulation or spontaneous mode. In the stimulation mode, a single pulse of 60 V/0.5 ms is applied using a Grass S48 Stimulator, 1 s after baseline fluorescence acquisition. After acquiring time-series images from all four FOVs, the electrode is retracted and the XY stage moves to position the center of the next well along the light path. This process is repeated until images have been acquired from all 96 wells. The use of a single electrode, instead of multi-well electrode assemblies [12-14], ensures consistent stimulus delivery across wells. A single plate can be screened in under 2 h 15 min.

Data analysis and storage. The time-series images from individual FOVs are analyzed in parallel to image acquisition, using a separate virtual instrument also written using LabView®. A thresholding algorithm identifies all fluorescent cells in a FOV. We use a complementary color NLS-FP reporter (eg. NLS-mCherry for ArcLight) for cell identification. To identify transfected cells, an intensity thresholding is applied, with a thresholding value of 1.5 times the mean intensity of the fluorescence image prior to stimulation. Pixel dilation is applied to cover entire somata. A mask image is created where each identified cell is tagged and converted to an individual region of interest (ROI). This mask image is used to extract the mean fluorescence intensity from the time series images. The dark frame value, collected when the light source is turned OFF, is subtracted from the mean intensity trace. The resting fluorescence value (F_0) is calculated by averaging the mean intensity values prior to stimulation. The percentage change in fluorescence at time *t* is obtained using the formula

$$\frac{\Delta F}{F_0}\% = \frac{F(t) - F_0}{F_0} x\ 100$$

Image acquisition from at least four FOVs per well allows us to record from as many as 500 cells per mutant. Since each plate is in turn tested in quadruplicates, the *n* increases to ~2000 cells per variant. After each round of screening, representative fluorescence snapshots of the cells, as well as the analyzed traces, are stored in our local server. The maximum response value ($\Delta Fmax$) from among all the analyzed traces, for each mutant, is manually picked out by a blinded researcher. These values are entered in a database created using FileMaker. The database also contains information on the wells (identifier, mutation), specimen plate (identifier, library information, date of plasmid prep) and experiment (identifier, dates of transfection and screening). The exact mutation in each well remains unknown until after the screening, when the plasmid library is sent for DNA sequencing (Keck DNA sequencing facility, Yale University).

System sensitivity. The sensitivity of our screening platform was evaluated by calculating the Z-score, a commonly used metric in high-throughput screening systems [15]. We screened several plates that contained both positive (ArcLight) and negative (non-performing GEVI) controls. The Z-score was calculated using the formula

$$Z\ score = 1 - \frac{3(\sigma_p + \sigma_{n)}}{|\mu_p - \mu_n|}$$

where σ and μ represent the standard deviation and mean of the positive (p) and negative (n) controls, respectively. With quadruplicate testing of sample plates, our system can detect as little as 3% changes in voltage sensitivity and exhibits a Z-score of 0.65, which indicates an excellent assay [15]. We routinely screen up to five plates a day, which translates to a throughput of about 480 variants/day. As we image ~500 cells per well, we achieve a sample content *n* of ~500*4=2000 cells/variant (Supplementary Fig. 1).

Supplementary Note 2

Improving the voltage sensitivity of FlicR1. FlicR1, a fusion of *Ci*VSD and circular-permuted (cp) mApple, is the only red GEVI with a moderate sensitivity and kinetics suitable for AP detection in neurons that is also imageable under relatively modest illumination intensities (~100 mW mm^{-2}; ~10-100 times < opsin-imaging intensities [16,17]). Unlike most GEVIs, FlicR1 shows a positive voltage-fluorescence relationship, exhibiting an increase in fluorescence during depolarization [18]. When we performed site-directed saturation mutagenesis of select residues on the FP barrel (1632 variants), followed by voltage screening on our platform, we identified two mutations G287E and K294I that, in combination, more than doubled FlicR1's voltage sensitivity (Supplementary Fig. 2). We validated the improved variant in combined patch-clamp and fluorescence imaging experiments in HEK cells (50 mW mm^{-2}, 561 nm laser), where we found that FlicR2 indeed exhibited a two-fold increase in sensitivity to depolarizing voltage steps compared to FlicR1 ($\Delta F/F$ for a 120 mV step of 12.9 ± 1.3%, n=6 cells versus 6.4 ± 1.0%, n=4 cells). However, both FlicR1 and FlicR2 were only marginally responsive to hyperpolarizing potentials. Further, the improved variant continued to exhibit dim fluorescence and intracellular aggregates, not unlike its predecessor [18]. In thick tissues, such as acute brain slices, FlicRs required higher illumination intensities to be visible and displayed punctate expression (Supplementary Fig. 2f). Since continuous high-power illumination can generate excessive heat and temperature increases at the specimen, which can in turn lead to photodamage of intact tissue [19], we reasoned that FlicR may not be compatible for live animal imaging.

11.   Kralj, J.M., Hochbaum, D.R., Douglass, A.D. & Cohen, A.E. Electrical spiking in Escherichia coli probed with a fluorescent voltage-indicating protein. *Science* **333**, 345-348 (2011).

12.   Huang, C.J. et al. Characterization of voltage-gated sodium-channel blockers by electrical stimulation and fluorescence detection of membrane potential. *Nature biotechnology* **24**, 439-446 (2006).

13.   Muller, O. et al. A system for optical high resolution screening of electrical excitable cells. *Cell calcium* **47**, 224-233 (2010).

14.   Wardill, T.J. et al. A neuron-based screening platform for optimizing genetically-encoded calcium indicators. *PloS one* **8**, e77728 (2013).

15.   Zhang, J.H., Chung, T.D. & Oldenburg, K.R. A Simple Statistical Parameter for Use in Evaluation and Validation of High Throughput Screening Assays. *Journal of biomolecular screening* **4**, 67-73 (1999).

16.   Flytzanis, N.C. et al. Archaerhodopsin variants with enhanced voltage-sensitive fluorescence in mammalian and Caenorhabditis elegans neurons. *Nature communications* **5**, 4894 (2014).

17.   Hochbaum, D.R. et al. All-optical electrophysiology in mammalian neurons using engineered microbial rhodopsins. *Nature methods* **11**, 825-833 (2014).

18.   Abdelfattah, A.S. et al. A Bright and Fast Red Fluorescent Protein Voltage Indicator That Reports Neuronal Activity in Organotypic Brain Slices. *J Neurosci* **36**, 2458-2472 (2016).

19.   Stujenske, J.M., Spellman, T. & Gordon, J.A. Modeling the Spatiotemporal Dynamics of Light and Heat Propagation for In Vivo Optogenetics. *Cell reports* **12**, 525-534 (2015).